JOURNAL OF MATERIALS SCIENCE 16 (1981) 3171–3182

Application of deformation mechanism maps to the study of high-temperature creep of a precipitate-free 25wt%Cr-20wt%Ni austenitic stainless steel

Y. TAKAHASHI, T. YAMANE
Department of Materials Science and Engineering, Osaka University, Suita 565, Japan

Deformation mechanism maps for a precipitate-free 25 wt % Cr–20 wt % Ni austenitic stainless steel are introduced with normalized stress, reciprocal of homologous temperature and normalized grain size as co-ordinate axes. The maps are plotted, using experimental results wherever possible rather than comparing constitutive strain-rate equations predicted by deformation mechanisms. The maps make it possible to systematically classify the complex creep behaviour of the stainless steel, so that transitions in creep behaviour with changes in stress, temperature and grain size are clearly revealed. It is indicated that, if the maps are prepared from the constitutive equations alone, they are not in agreement with the experimental results.

1. Introduction

It has been recognized that several deformation mechanisms contribute towards creep deformation of a polycrystalline solid, and each depend on stress, temperature, and material structure such as grain size. It is thus necessary in studies of high-temperature creep to identify the dominant mechanism under any particular experimental conditions.

In 1965, the idea of a "creep diagram" was originally proposed by Weertman and Weertman [1, 2]. The idea was developed by Ashby [3], who produced "deformation mechanism maps" for several pure metals and ceramics. Since then, various types of deformation mechanism maps have been produced by a number of authors, especially Langdon and Mohamed [4–11], for the purpose of displaying information about creep behaviour more clearly. Now, it is widely accepted that the deformation mechanism maps are a simple but powerful tool for comprehending high-temperature creep behaviours which seem to be complicated.

The steady-state creep in a 25 wt % Cr–20 wt % Ni austenitic stainless steel depends on stress, temperature and grain size [12–14]. It is, therefore, important to systematically classify creep behaviours, constructing two- and three-dimensional deformation mechanism maps with the normalized stress (σ/G), reciprocal of the homologous temperature (T_m/T) and the normalized grain size ($d/\mathbf{b}$), as co-ordinate axes, where σ is the applied stress, G is the shear modulus, T is the absolute temperature, T_m is the melting point of the material in Kelvin,* d is the mean grain diameter and $\mathbf{b}$ is the Burgers vector. The purpose of this paper is to gain some understanding of high-temperature creep of stainless steel using deformation mechanism maps, based, wherever possible, on our experimental results rather than on theoretical predictions.

2. Types of deformation mechanisms

High-temperature creep can arise in at least four different ways [2–4, 14, 17–19]: recovery-controlled creep; thermally-activated glide-

*For T_m of the stainless steel, an absolute solidus temperature in the equilibrium diagram of the Fe–Cr–Ni system [15, 16] was adopted.

0022–2461/81/113171–13$03.30/0

TABLE I Chemical composition (wt%) of a vacuum-melted stainless steel

Cr	Ni	C	Mn	Si	S	P
22.77	21.39	0.005	Nil	0.02	0.009	0.004

controlled creep; Coble creep and Nabarro–Herring creep.

In recovery-controlled creep, the rate controlling process is "recovery" of the dislocation-substructure by the climb motion of dislocations [2, 17, 20]. This type of creep is widely observed in pure metals [18, 19]. The rate-controlling process may be thermally-activated "glide" of dislocations. This mechanism can be further subdivided into two classes: viscous glide, G_1, and jerky glide, G_2. G_1 is controlled by jog- or solute-drag, so that volume- or solute-diffusion is required. G_2 is exclusively limited by localized obstacles and does not necessarily require the aid of diffusion. G_2 has been designated as "dislocation-glide" by Ashby [3], who suggests that it dominates in the normalized stress range from $(0.5 \sim 1.0) \times 10^{-2}$ to (σ_{th}/G), where σ_{th} is the theoretical shear strength for defectless flow, and nearly equal to $(3^{1/2}/20)G$.

Stress-induced vacancy transport permits creep deformation, as well as conservative motion of dislocations. If the transport is predominantly along grain boundaries, deformation is called Coble creep [21]. When, instead, bulk-transport dominates, it is known as Nabarro–Herring creep [22, 23].

The strain rates, $\dot{\epsilon}$, predicted by these deformation mechanisms can be expressed, except in the case of dislocation glide, G_2 [3, 4, 6, 20], in

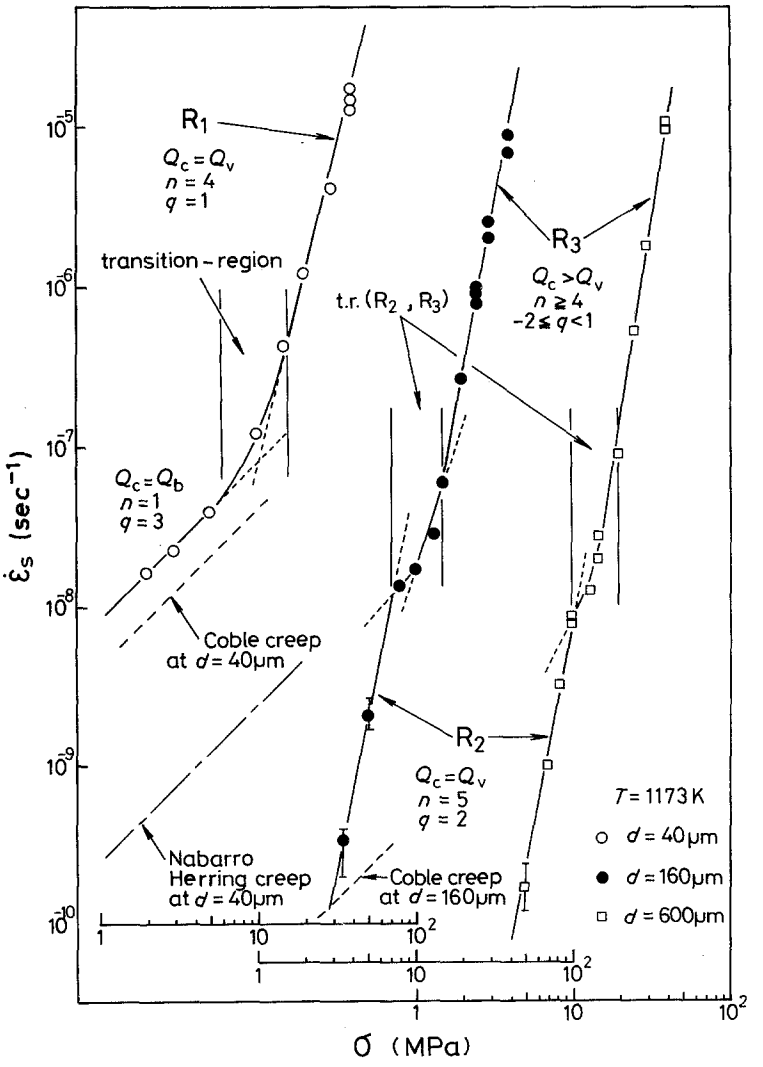

Figure 1 Stress dependence of the steady-state creep rates, $\dot{\epsilon}_s$. Coble creep (- - -) and Nabarro–Herring creep (——·——·——) are theoretical.

the form

$$\dot{\epsilon} = A\left(\frac{D_0 G\mathbf{b}}{kT}\right)(\sigma/G)^n(\mathbf{b}/d)^q \exp\left(-\frac{Q_c}{RT}\right), \quad (1)$$

where A is a dimensionless constant, D_0 is a frequency factor, k is Boltzman's constant, Q_c is an activation energy for creep, R is the gas constant, and n and q are the exponents for the stress and the inverse grain size, respectively.

If d and T are constant, recovery-creep gives $n = 3$ to 5, in contrast with viscous-glide, G_1, where $n \simeq 3$ is established [19]. Recovery-creep and G_1 are often called "power-law creep". Coble creep and Nabarro–Herring creep are linear functions of stress ($n = 1$) and are called "viscous creep".

For power-law creep with $T > 0.5T_m$ and Nabarro–Herring creep, then $D_0 \exp(-Q_c/RT) = D_{v0} \exp(-Q_v/RT) = D_v$, where D_v is the volume diffusion coefficient with a pre-exponential constant, D_{v0}, and an activation energy, Q_v. However, for Coble creep, $D_0 \exp(-Q_c/RT) = D_{b0} \exp(-Q_b/RT) = D_b$, where D_b is the grain-boundary diffusion coefficient with a pre-exponential constant, D_{b0}, and an activation energy, Q_b.†

With respect to the grain-size dependence of $\dot{\epsilon}$, Coble creep and Nabarro–Herring creep exhibit $q = 3$ and $q = 2$, respectively, and usually $q \sim 0$ is assumed for power-law creep. In practice, how-

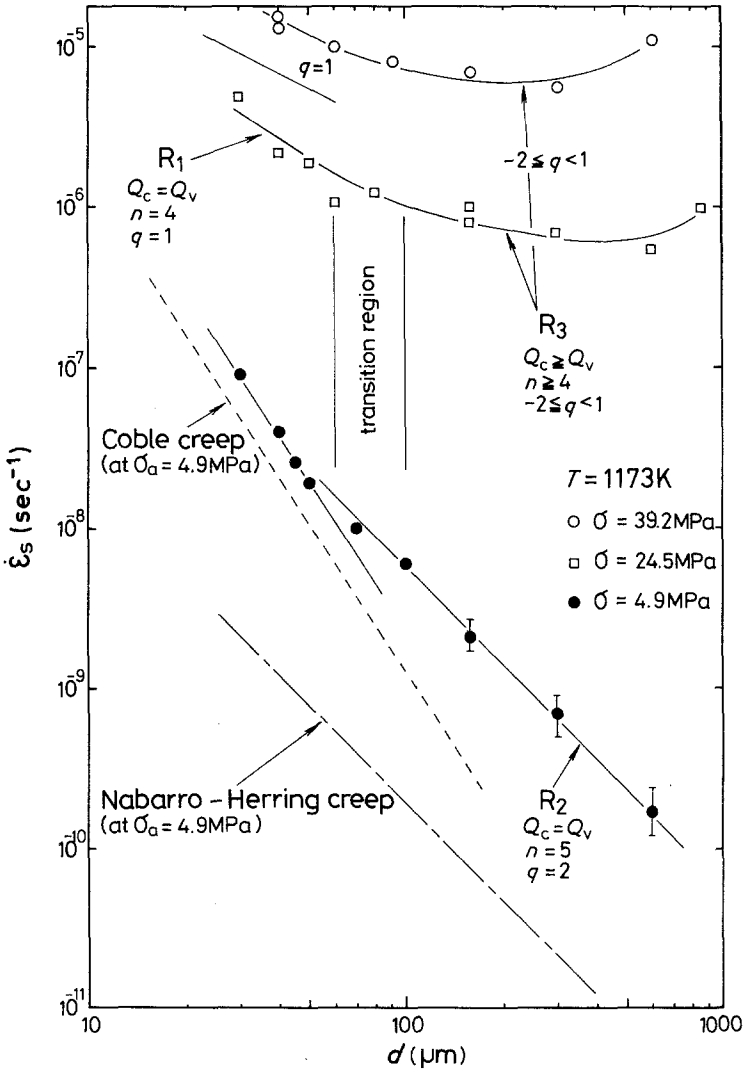

Figure 2 Grain-size dependence of $\dot{\epsilon}_s$.

†In this study, D_v and D_b approximate to the volume and the grain-boundary self-diffusion coefficients of Fe in the stainless steel, respectively.

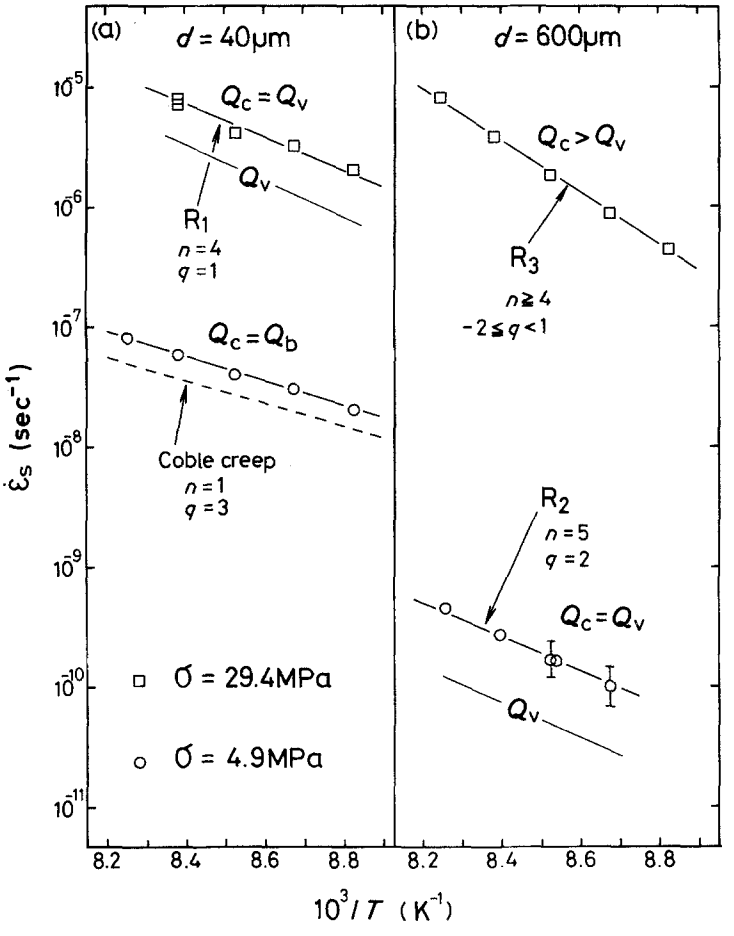

Figure 3 Temperature dependence of $\dot{\epsilon}_s$. The narrow temperature range permits the temperature dependence of the shear modulus, G, to be neglected.

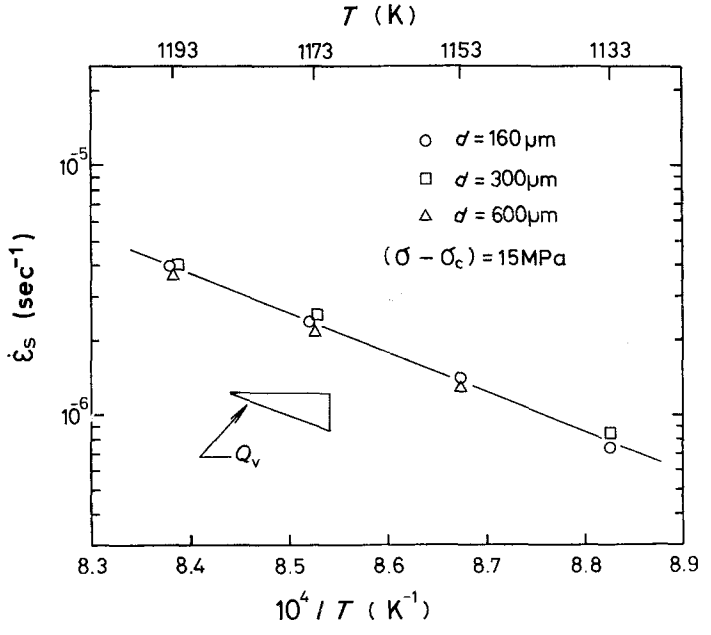

Figure 4 Temperature dependence of the steady-state creep rates for R_3, which are rearranged under the same conditions of $\sigma - \sigma_c$.

ever, power-law creep does depend on grain size [14, 25–26]. This immediately gives rise to a discrepancy between maps based on the constitutive equations for power-law creep and those based on experimental data [3–11]. It is, therefore, necessary to take the effect of grain size on power-law creep into consideration.

3. Experimental procedure

The material used in this study was vacuum-melted 25 wt% Cr–20 wt% Ni austenitic stainless steel, the compositions of which are shown in Table I. The experimental procedures have been detailed in previous work [12–14]. The test temperatures were $(0.65 \sim 0.75)T_m$, a range where carbide-precipitates and sigma-phase were absent.

4. Experimental results

Figs 1 to 3 show examples of the dependence of the steady state creep rates, $\dot{\epsilon}_s$, on stress, grain size and temperature, respectively. The power-law creep can be subdivided into three characteristics of R_1, R_2 and R_3. R_1 is observed for the fine-grained specimens ($d < 60\,\mu m$) and R_2 and R_3 for $d > 100\,\mu m$. It has been reported [14] that these three creep regimes are individually recovery-controlled. R_1 is gradually displaced by Coble creep with decreasing stress, whereas R_3 is found to be superseded by R_2 at $\sigma \simeq 10$ MPa, $T = 1173$ K ($\sigma/G \simeq 2 \times 10^{-4}$). The transition region from R_3 to R_2, tr(R_2, R_3), is considered to be the field of viscous glide, G_1, because $n \simeq 3$ is established and the creep curve exhibits an inverse-type primary

TABLE II Constitutive equations for creep deformation mechanisms and physical property values

Creep	Constitutive equation
R_1	$\dot{\epsilon} = 1.4 \times 10^8 \left(\frac{D_{v0} G b}{kT}\right)\left(\frac{\sigma}{G}\right)^4 \left(\frac{b}{d}\right) \exp\left(-\frac{Q_v}{RT}\right)$
R_2	$\dot{\epsilon} = 1.8 \times 10^{18} \left(\frac{D_{v0} G b}{kT}\right)\left(\frac{\sigma}{G}\right)^5 \left(\frac{b}{d}\right)^2 \exp\left(-\frac{Q_v}{RT}\right)$
R_3	$\dot{\epsilon} = 7.3 \times 10^3 \left(\frac{D_{v0} G b}{kT}\right)\left(\frac{\sigma - \sigma_c}{G}\right)^4 \exp\left(-\frac{Q_v}{RT}\right)$
G_1	$\dot{\epsilon} = A\left(\frac{D_{v0} G b}{kT}\right)\left(\frac{\sigma}{G}\right)^{\sim 3} \exp\left(-\frac{Q_v}{RT}\right)$
G_2	$\dot{\epsilon} = \dot{\epsilon}_0 \exp\left[-(\Delta F/kT)\left(1 - \frac{\sigma}{\sigma_{f0}}\right)\right]$, where $\dot{\epsilon}_0$ is an appropriate pre-exponential term, ΔF is the free energy necessary to overcome the obstacle and σ_{f0} is the flow stress at 0 K.
Coble creep	$\dot{\epsilon} = 14 \cdot \frac{\pi\delta}{b^2}\left(\frac{D_{b0} G b}{kT}\right)\left(\frac{\sigma}{G}\right)\left(\frac{b}{d}\right)^3 \exp\left(-\frac{Q_b}{RT}\right)$, where δ is the effective grain-boundary width.
Nabarro–Herring creep	$\dot{\epsilon} = 14 \cdot \frac{\Omega}{b^3}\left(\frac{D_{v0} G b}{kT}\right)\left(\frac{\sigma}{G}\right)\left(\frac{b}{d}\right)^2 \exp\left(-\frac{Q_v}{RT}\right)$, where Ω is the atomic volume.

Note: The equations for R_1, R_2 and R_3 are based on our experimental results, but those of G_1 and G_2 are probable ones [9, 19]. Those of Coble creep and Nabarro–Herring creep are theoretical [3].

Physical property values

$D_{v0} = 1.74 \times 10^{-4}$ m^2 sec^{-1}
$\delta D_{b0} = 8.30 \times 10^{-13}$ m^3 sec^{-1}
$Q_v = 285$ kJ mol^{-1}
$Q_b = 180$ kJ mol^{-1}
$\Omega = 1.21 \times 10^{-29}$ m^3
$b = 3.0 \times 10^{-10}$ m
$T_m = 1696$ K

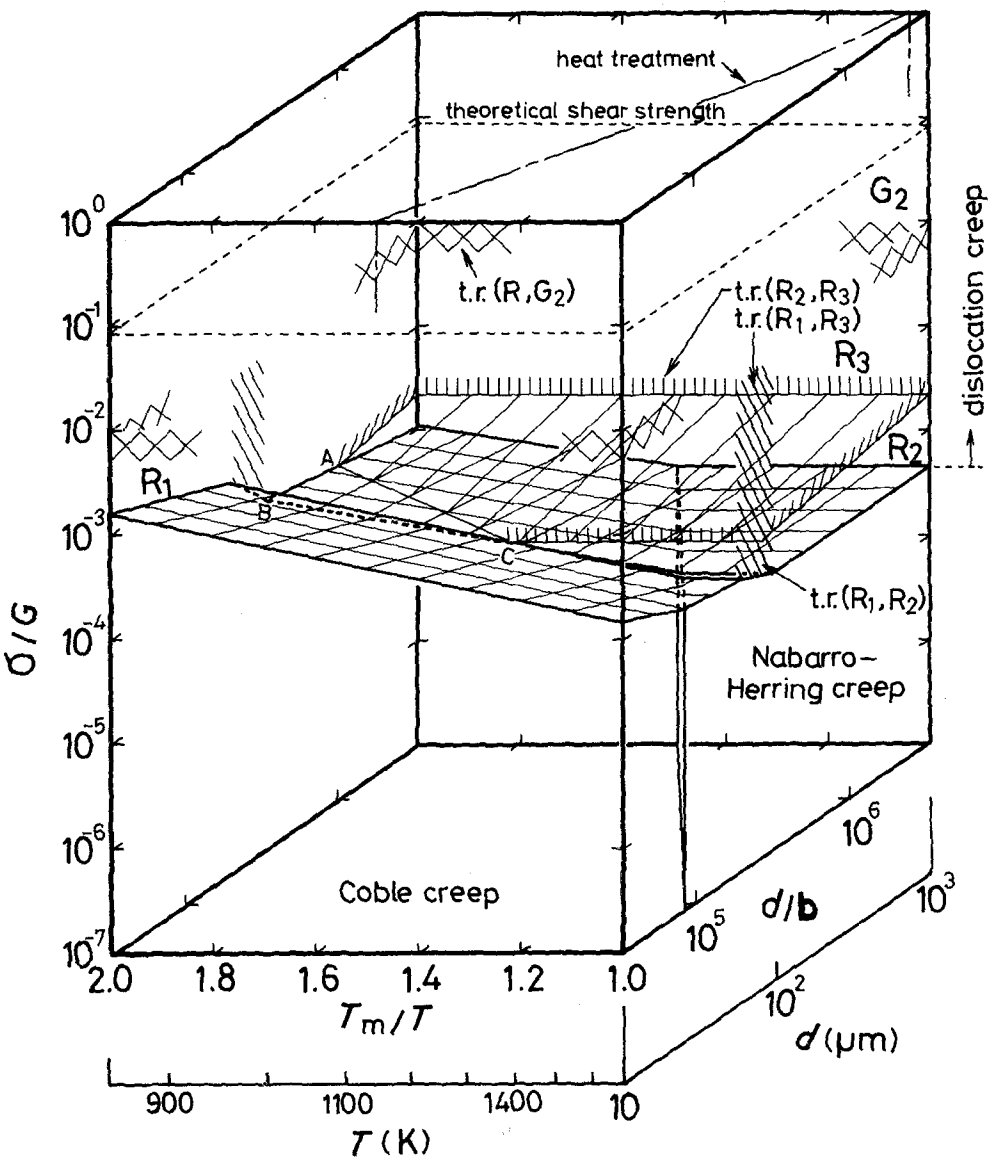

Figure 5 A three-dimensional map. The transition region from recovery creep (R_1 or R_3) to G_2, tr(R, G_2), is expressed as a symbol of XXX.

creep in tr(R_2, R_3) [12, 19]. In R_3, although $Q_c > Q_v$ is shown, $Q_c \simeq Q_v$ can be established by introducing the strain-arrest stress, σ_e (cf. Fig. 4). σ_e has been defined in previous work [13, 14]. R_3 is essentially independent of grain size [14]. It is considered that R_3 is strongly associated with the formation of dislocation-substructure [14, 25]. The range of d from 60 to 100 μm can be regarded as the transition region from R_1 to R_3, tr(R_1, R_3).

5. The method of mapping

Table II shows the constitutive equations for the creep deformation mechanisms which have been considered in this report. It also gives physical property values. Deformation mechanism maps were constructed by the following seven-step procedure.

(1) A three-dimensional space with the coordinates, (σ/G), (T_m/T) and (d/b) was prepared. The space was limited by letting (σ/G) range from 10^{-7} to 10^0, (T_m/T) range from 1.0 to 2.0, and (d/b) range from 3.3×10^4 to 3.3×10^6 (comparable to $d = 10$ to 1000 μm).

(2) The space was separated into two parts at $(d/b) = 2.7 \times 10^5$ ($d = 80\,\mu$m). One of them was prepared to construct a map for $d \leqq 60\,\mu$m, and the other to construct a map for $d \geqq 100\,\mu$m.

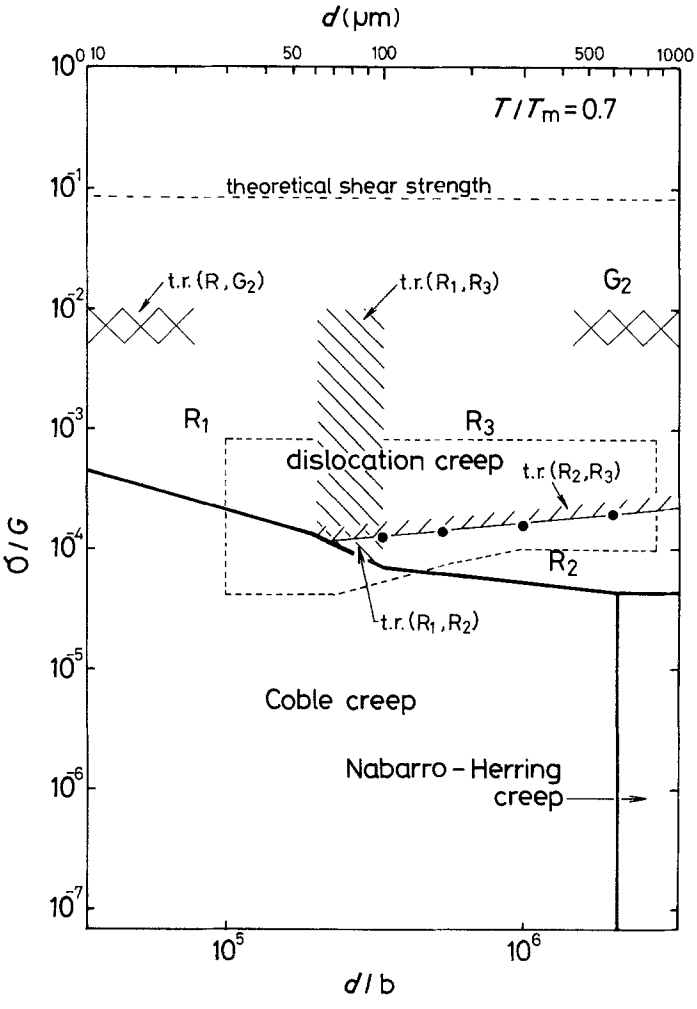

Figure 6 A (σ/G)–(d/b) diagram for $T = 0.7T_m$.

(3) In mapping for $d \leqq 60\,\mu$m; R_1, Coble creep and Nabarro–Herring creep were initially considered. It was assumed that, of these three, the mechanism which supplies the largest strain rate at a point, $(\sigma/G, T_m/T, d/\mathrm{b})$ is the dominant mechanism at that point. Domain-boundaries were obtained by equating pairs of the constitutive equations.

(4) In mapping for $d \geqq 100\,\mu$m; R_2, R_3, Coble creep and Nabarro–Herring creep were considered. The domains and the domain-boundaries were estimated in a similar manner to Ashby [3] but using the condition that R_2 is displaced by R_3 above a critical value of (σ/G) corresponding to $\mathrm{tr}(R_2, R_3)$.

(5) The domain of dislocation-glide, G_2, was empirically drawn, according to other deformation mechanism maps, for instance, maps for 18 wt% Cr–8 wt% Ni stainless steels [27, 28].

(6) The two parts which had separately been mapped were unified into a three-dimensional diagram.

(7) Two-dimensional maps were drawn as sections of the three-dimensional diagram. The shear modulus, G, is given by

$$G = 8.3 \times 10^{10} - 3.0 \times 10^{7} T. \qquad (2)$$

Equation 2 was approximated as $G = E/2(1 + \nu)$ assuming $\nu = 1/3$ and the same temperature dependence as Young's modulus, E, using the data of Nortetiffe [29].

6. A three-dimensional map

A three-dimensional map is shown in Fig. 5. Six different mechanisms are represented as domains (fields): dislocation-glide, G_2; the three different recovery-creep regions, R_1, R_2 and R_3; Coble creep; and Nabarro–Herring creep. The field of G_1 is shown as $\mathrm{tr}(R_2, R_3)$. The unified domain with R_1, R_2 and R_3 is similar, or may be compar-

able to that of dislocation creep which has already been presented by several authors [3–11, 27, 28]. This map makes it possible to identify the dominant mechanism during steady-state creep under any conditions of (σ/G, T_m/T, d/b) and also identifies transitions of mechanism through domain-boundaries, for example, between Coble creep and Nabarro–Herring creep. It is represented as a "plane" parallel to the (σ/G) axis but not to the (T_m/T) axis or the (d/b) axis. This means that the transition between Coble creep and Nabarro–Herring creep occurs with changes in temperature and grain size but not with changes in stress.

When these maps are used to predict creep behaviour, it is important to recognize the possibility of changes in grain size during creep. Such changes can also be represented in the maps. Heat-treatment temperatures for each grain size are indicated at the top of the map in Fig. 5. The curve gives information about the grain growth during creep. It can be indicated in the temperature range above the heat-treatment temperatures that crystal grains must grow during creep.

The field of ΔABC in Fig. 5 represents the domain-boundary between Coble creep and R_2, although the R_2-domain seems to disappear. This delta-field results from $\mathrm{tr}(R_2, R_3)$ estimated with the experimental results at $T = (0.65 \text{ to } 0.75)T_m$. The strain rates in the delta-field are too small to precisely estimate $\mathrm{tr}(R_2, R_3)$, but it is considered that in the delta-field there exists a possibility of $\mathrm{tr}(R_2, R_3)$ expanding, so that, with increasing stress, Coble creep is gradually replaced by R_3 through R_2 or G_1.

7. Two-dimensional maps

The three-dimensional map gives the overall picture of the dominant regions of the deformation mechanisms. Two-dimensional maps can also give a good deal of information about the creep behaviour of the stainless steel for specific cases.

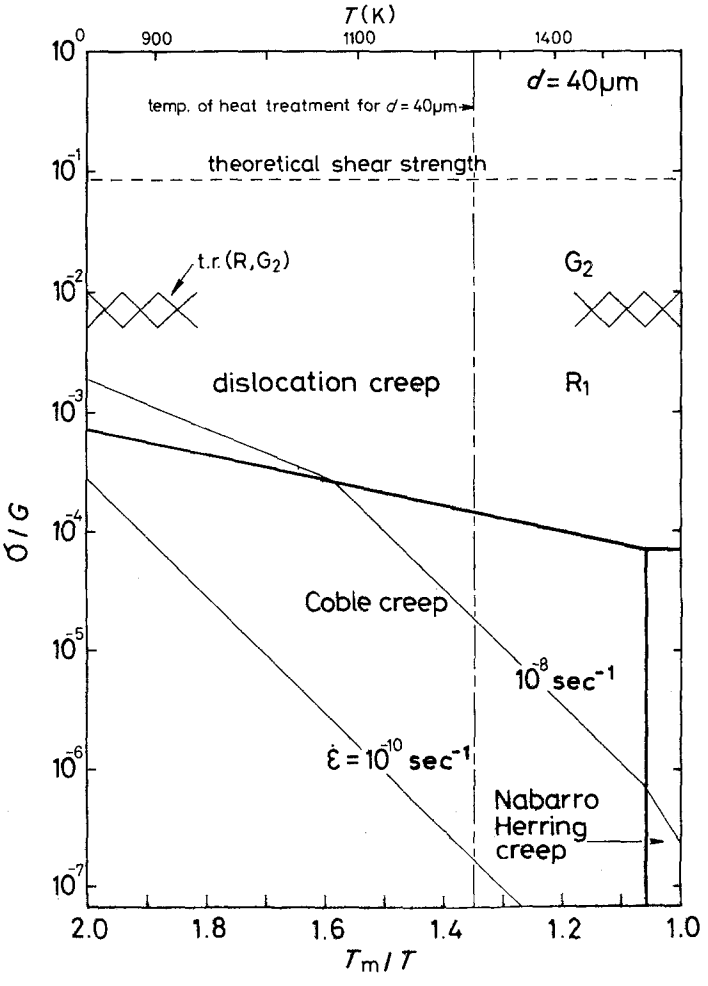

Figure 7 A (σ/G)–(T_m/T) diagram for $d = 40\,\mu m$.

7.1. A (σ/G)–(d/b) diagram

In Fig. 6, a (σ/G)–(d/b) diagram at $T = 0.7T_m$ is shown. The field surrounded by a dotted line has been examined. Solid points are experimental values of $\mathrm{tr}(R_2, R_3)$. It is suggested that $\mathrm{tr}(R_2, R_3)$ is comparable to the domain of viscous glide, G_1. In the R_2 domain, the rate of recovery is considered so slow that the time necessary for viscous gliding of a dislocation may be negligible in discussing the rate-controlling process [30].

7.2. (σ/G)–(T_m/T) diagrams

Figs 7 to 9 show examples of (σ/G)–(T_m/T) diagrams, together with contours of constant strain rates, $\dot{\epsilon}$. These contours have been drawn, assuming that $\dot{\epsilon}$ in each domain is contributed to only by the dominant mechanism. It appears from these contours that Coble creep for $d > 160\,\mu m$ is difficult to observe, because $\dot{\epsilon} < 10^{-10}\ \mathrm{sec}^{-1}$ is not detectable. Similarly, it is indicated that Nabarro–Herring creep can be observed only at temperatures just below T_m.

In Fig. 8, the R_2 domain diminishes above $T_m/T = 1.8$, but this zone is comparable to a section of ΔABC in Fig. 5. It may be regarded as the expanded $\mathrm{tr}(R_2, R_3)$.

7.3. (T_m/T)–(d/b) diagrams

(T_m/T)–(d/b) diagrams in Fig. 10 give information on the transition of creep deformation mechanisms with change in normalized stress, σ/G. At $\sigma/G < 4.3 \times 10^{-5}$ (Fig. 10a), only vacancy creep such as Coble and Nabarro–Herring occurs. Coble creep dominates at low temperatures and fine grain sizes. When σ/G is increased to 4.3×10^{-5} (Fig. 10b), recovery creep, R_2, appears at high

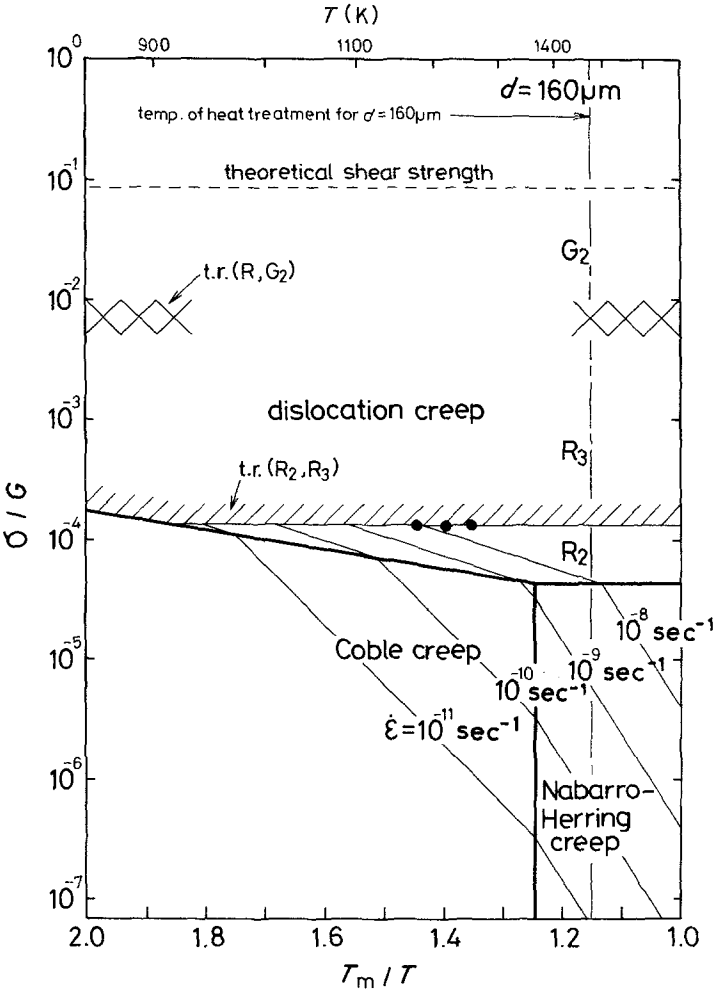

Figure 8 A (σ/G)–(T_m/T) diagram for $d = 160\,\mu m$.

temperatures and coarse grain sizes. Then, R_1 appears at $\sigma/G = 6.0 \times 10^{-5}$ (Fig. 10c). When σ/G is increased still more (Fig. 10d), Nabarro–Herring creep can no longer dominate, even if $d/\mathbf{b}$ and T_m/T are changed over the full scales. At $\sigma/G = 2.0 \times 10^{-4}$ (Fig. 10e), R_3 appears at middle grain sizes. In the range of σ/G above 1.8×10^{-3}, Coble creep vanishes from the map (Fig. 10f), and then recovery creep is dominant. The recovery creep has different characteristics, that is, R_1 in $d < 60\,\mu m$ and R_3 in $d > 100\,\mu m$. The division of R_1 and R_3 is supported by the fact that the high-temperature creep is affected by the dislocation substructure such as sub-boundaries as well as by grain size [20, 24, 25, 31, 32]. R_1 and R_3 are gradually changed into dislocation-glide, G_2, with increasing σ/G. This transition region, tr(R, G_2), may be understood as the field of so-called "glide-recovery creep" [33]. According to other studies [34, 35], in the range $T < 0.6T_m$, tr(R, G_2) is let down to $\sigma/G \simeq 2.0 \times 10^{-3}$. Also, the recovery creep at $T < 0.6T_m$ may be controlled by dislocation-core diffusion.

In this report, it has been naturally assumed that the experimental results in $T = (0.65 \sim 0.75)T_m$ can be successful all over the range, by using (σ/G), (T_m/T) and $(d/\mathbf{b})$ scales [1–3]. It should be kept in mind that the maps are limited to the steady-state flow, and time-dependent effects are not included, except for the grain-growth.

8. Discussion

The construction of the maps largely depends on our experimental data. If the construction is only based on the comparison of the strain rates, the maps would be in contradiction with the experimental results, for instance, R_1 could be compared with R_2.

Now, it is supposed that R_1 and R_2 independently contribute to the total creep strain rate at any points, $(\sigma/G, T_m/T, d/\mathbf{b})$. In the field where

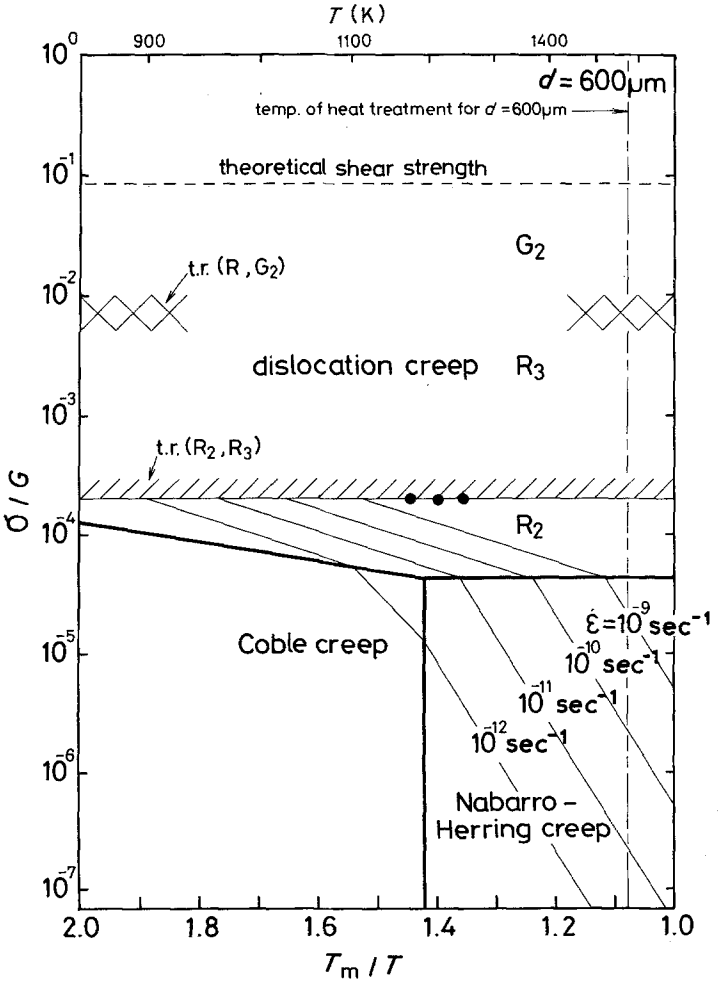

Figure 9 A (σ/G)–(T_m/T) diagram for $d = 600\,\mu m$.

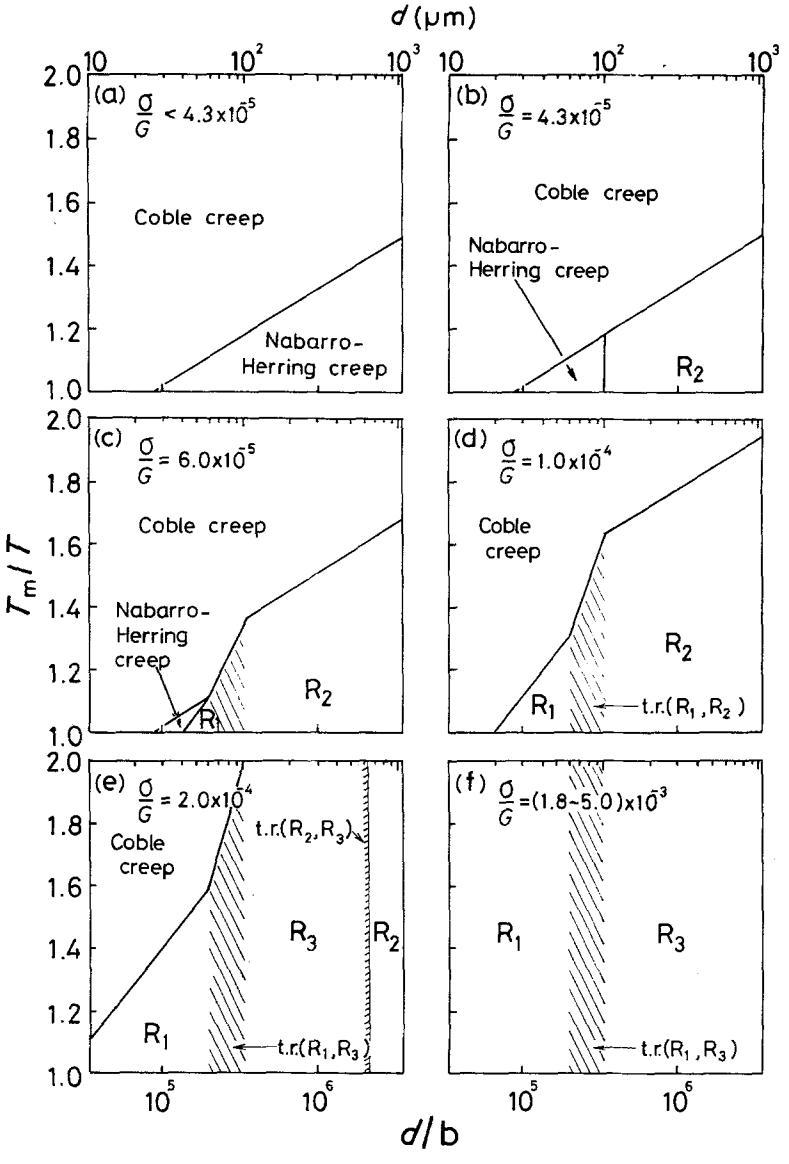

Figure 10 (T_m/T)–(d/b) diagrams: (a) $\sigma/G < 4.3 \times 10^{-5}$; (b) $\sigma/G = 4.3 \times 10^{-5}$; (c) $\sigma/G = 6.0 \times 10^{-5}$; (d) $\sigma/G = 1.0 \times 10^{-4}$; (e) $\sigma/G = 2.0 \times 10^{-4}$; (f) $\sigma/G = (1.8 \text{ to } 5.0) \times 10^{-3}$.

the strain rate, $\dot{\epsilon}_1$, of R_1 is larger than that, $\dot{\epsilon}_2$, of R_2, the following inequality is necessary to be established.

$$\dot{\epsilon}_1 \geqq \dot{\epsilon}_2. \quad (3)$$

From the constitutive equations listed in Table II,

$$\log(\sigma/G) \leqq \log(d/b) - 10.12. \quad (4)$$

According to this inequality, it is impossible for the R_1 domain shown in Fig. 5 to exist. For example, in Fig. 5, a point of $(\sigma/G, T_m/T, d/b) = (5 \times 10^{-4}, 1.43, 1.2 \times 10^5)$‡ does not satisfy the inequality in Equation 4. The creep behaviour ascribed to R_1 can, however, be observed under the same condition (cf. Figs 1 to 3). It is, therefore, found that R_1 and R_2 are not independent, but only alternative mechanisms to each other, as likely as R_1 and R_3. However, vacancy creep without the conservative motion of a dislocation can be expected to be independent of R_1, R_2 and R_3. It is also considered that Coble creep and Nabarro–Herring creep are independent of each other, since they are obviously different in the path of the transport. There remains a problem as to vacancy creep: Bingham behaviour (threshold stress) [36, 37]. If this problem is taken into consideration, it is expected that the maps will aid classification of the high-temperature creep behaviour of stainless steel still more.

‡This condition is equivalent to $T = 1173$ K, $\sigma = 25$ MPa and $d = 40\,\mu$m.

9. Conclusions

(1) The high-temperature creep behaviour of a precipitate-free 25 wt% Cr–20 wt% Ni austenitic stainless steel is broadly classified into seven groups: three characteristic recovery creeps of R_1, R_2 and R_3; two different thermally-activated creeps of G_1 and G_2; Coble creep; and Nabarro–Herring creep.

(2) These creep mechanisms are plotted as domains in a three-dimensional deformation mechanism map with co-ordinates, (σ/G), (T_m/T) and (d/b).

(3) The three-dimensional map makes it possible not only to easily recognize the dominant mechanism under any conditions of $(\sigma/G, T_m/T, d/b)$, but also to predict the possibility of the transition of these mechanisms with change in stress, temperature and grain size.

(4) It is necessary in mapping to take note of the grain-size effect on recovery creep.

(5) The deformation mechanism maps should be plotted using experimental results wherever possible rather than comparing constitutive strain-rate equations.

References

1. J. WEERTMAN and J. R. WEERTMAN, "Physical Metallurgy", edited by R. W. Cahn (North-Holland, Amsterdam, 1965) p. 793.
2. J. WEERTMAN, *Trans. ASM* **61** (1968) 681.
3. M. F. ASHBY, *Acta Met.* **20** (1972) 887.
4. F. A. MOHAMED and T. G. LANGDON, *Met. Trans.* **5** (1974) 2339.
5. *Idem, Scripta Met.* **9** (1975) 137.
6. T. G. LANGDON and F. A. MOHAMED, *Mater. Sci. Eng.* **32** (1978) 103.
7. *Idem, J. Mater. Sci.* **13** (1978) 473.
8. *Idem, ibid.* **13** (1978) 1282.
9. R. N. SINGH, *J. Nucl. Mater.* **64** (1977) 167.
10. H. OIKAWA, *Scripta Met.* **13** (1979) 701.
11. *Idem, Mater. Sci. Eng.* **45** (1980) 211.
12. Y. TAKAHASHI and T. YAMANE, *J. Mater. Sci.* **14** (1979) 2818.
13. Y. TAKAHASHI, K. NAKAGAWA and T. YAMANE, *Z. Metallk.* **71** (1980) 572.
14. Y. TAKAHASHI and T. YAMANE, *J. Mater. Sci.* **16** (1981) 397.
15. J. H. PUGH and J. D. NISBET, *J. Met.* **2** (1950) 268.
16. P. SCHAFMEISTER and P. ERGANG, *Arch. Eisen* **12** (1938–9) 459.
17. J. P. POIRIER, *Acta Met.* **25** (1977) 913.
18. S. TAKEUCHI and A. S. ARGON, *J. Mater. Sci.* **11** (1976) 1542.
19. F. A. MOHAMED and T. G. LANGDON, *Acta Met.* **22** (1974) 779.
20. J. WEERTMAN, "Rate Processes in Plastic Deformation of Materials", Vol. 4 (American Society for Metals, Metals Park, Ohio, 1975) p. 315.
21. R. L. COBLE, *J. Appl. Phys.* **34** (1963) 1679.
22. C. HERRING, *ibid.* **21** (1950) 437.
23. F. R. N. NABARRO, Report of Conference of Strength of Solids (Physical Society, London, 1948) p. 75.
24. F. GAROFALO, W. F. DOMIS and F. VON GEMMINGEN, *Trans. AIME* **230** (1964) 1460.
25. O. D. SHERBY, *Acta Met.* **10** (1962) 135.
26. Y. IMAI and T. MURATA, *Jap. Inst. Met.* **6** (1967) 585.
27. J. H. GITTUS, *Phil. Mag.* **30** (1974) 751.
28. F. R. BECKITT, T. M. BANKS and T. GLADMAN, "Creep Strength in Steel and High-Temperature Alloys" (The Metals Society, London, 1974) p. 71.
29. R. NORTELIFFE, *J. Iron Steel Inst.* **157** (1947) 345.
30. H. OIKAWA, K. SUGAWARA and S. KARASHIMA, *Trans. JIM* **19** (1978) 611.
31. O. AJAJA and A. J. ARDELL, *Phil. Mag.* **A39** (1979) 65.
32. O. D. SHERBY and P. M. BURKE, "Progress in Materials Science", Vol. 13 (Pergamon Press, London, 1966) p. 325.
33. U. F. KOCKS, "Rate Processes in Plastic Deformation of Materials", Vol. 4 (American Society for Metals, Metals Park, Ohio, 1975) p. 356.
34. R. LAGNEBORG, *Met. Sci. J.* **6** (1972) 127.
35. O. K. CHOPRA and K. NATESAN, *Trans. Met.* **8A** (1977) 633.
36. T. SRITHHARAN and H. JONES, *Acta Met.* **28** (1980) 1633.
37. B. BURTON and G. L. REYNOLDS, *Scripta Met.* **13** (1979) 839.

Received 19 March and accepted 30 April 1981.